Contents lists available at ScienceDirect

Commun Nonlinear Sci Numer Simulat

Research paper

Alternating superlattice textures in driven nanomagnets

CrossMark

Alejandro O. Leon [a,b,*], David Laroze [c], Marcel G. Clerc [b], Ana M. Cabanas [c]

[a] *Institute for Materials Research, Tohoku University, Sendai 980-8577, Japan*
[b] *Departamento de Física, Facultad de Ciencias Físicas y Matemáticas, Universidad de Chile, Casilla 487-3, Santiago, Chile*
[c] *Instituto de Alta Investigación, Universidad de Tarapacá, Casilla 7D, Arica, Chile*

ARTICLE INFO

ABSTRACT

Nanomagnets driven with uniform electric currents exhibit a wide variety of spatial textures. In the present work, we investigate alternating superlattice states in nanomagnets, which are spatially periodic textures composed by several spatial modes that oscillate in time. The magnetic system is described in the continuum approach by the Landau–Lifshitz–Gilbert–Slonczewski equation, and direct numerical simulations of this model allow us to characterize the alternating patterns. As a result of this temporal oscillation, textures alternate between different shapes. In particular, we focus on two types of textures, namely a superhexagon and a square-like pattern, which are composed by six and two dominant Fourier modes, respectively. Based on an appropriate modal decomposition, we reveal that the mechanism that originates the alternating superhexagon is a homoclinic bifurcation. In addition, we show that the oscillatory square-like texture emerges through a supercritical Andronov–Hopf bifurcation.

© 2016 Elsevier B.V. All rights reserved.

1. Introduction

Macroscopic systems exhibit spatial patterns as a result of the competition between dissipation and injection of energy, momentum and particles [1,2]. Examples of patterns can be found in different branches of science and within a wide range of spatial scales, such as stripes in zebra's skin, ocean waves, vegetal population spots, sand ripples, convection rolls in fluids, to mention a few. From the mathematical point of view, regular patterns are spatially periodic states composed by spatial modes with one or a few intrinsic wavenumbers [2]. At the onset of the spatial bifurcation that originates the patterns, the dynamical evolution of the system is governed by the critical modes of the instability, while all the other degrees of freedom are slave variables and then they are functions of the critical modes. In two spatial dimensions, the most common observed patterns are stripes (one roll-like mode), squares (two roll-like modes), and hexagons (three roll-like modes). On the other hand, superlattices are an example of more sophisticated structures because they are composed by at least four interacting modes [2]. The analytical description of pattern forming systems is usually performed by means of amplitude equations [1]. This approach permits predicting the shape of the pattern and obtaining simple mathematical expressions for the mode envelopes as functions of the physical parameters of the system. In the case of stationary spatial instabilities, amplitude equations usually take the form of relaxation equations, and therefore they only predict steady states.

When the energy injection is increased, stationary patterns might become dynamic states, which is a secondary bifurcation of the system [1]. An example of dynamic textures is alternating patterns, in which the dissipative structure oscillates

---

* Corresponding author.
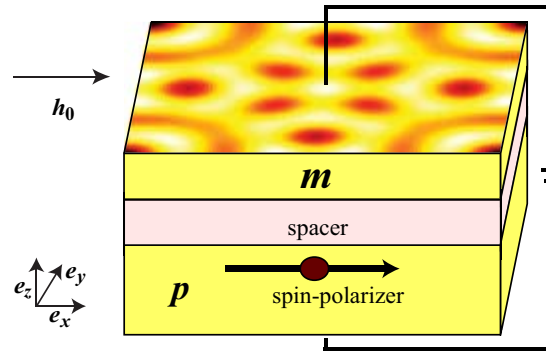 *E-mail address:* aoleon@imr.tohoku.ac.jp (A.O. Leon).

Fig. 1. Spin-valve device composed by two ferromagnets and one spacer. The thicker material with *fixed* magnetization **p** polarizes or filters the spins of the electric current, while the other ferromagnetic layer with *free* magnetization **m** interacts with the current and the external field **h₀**; we are interested in the dynamics of this magnet. The two materials are separated by a nonmagnetic metal to avoid magnetostatic interactions between them. The rest of the structure (not shown) is composed by non-magnetic metals.

in time, and the envelopes of spatial modes alternate between large and small values. Alternation between simple lattices were observed in Rayleigh–Bénard experiments [3,4], where a fluid mixture is heated from below and cooled from the top. In this case, the fluid alternates between two types of convection patterns, namely rolls and squares, as a result of a supercritical Andronov–Hopf instability of a stationary square texture. This type of secondary bifurcation is described by the well known Ginzburg–Landau equation, however the derivation of this equation requires to know the analytical expression of the stationary pattern, which is usually unknown. Therefore, the derivation of the corresponding amplitude equations is a complicated task. An alternative strategy to study secondary instabilities is by means of a truncated modal decomposition of the equations into an arbitrary number of modes, this approach is known as the Galerkin expansion. For the case of Rayleigh–Bénard experiment, the alternating patterns were studied theoretically using the Galerkin method [5]; which permitted transforming of the spatiotemporal dynamics into a set of Lorentz-type equations, where the analytical calculations and the numerical characterization become easier. During last decade, several other examples of alternating patterns have been observed and studied in the context of fluid convection [6–12]; the mechanisms that originate the oscillatory states are homoclinic bifurcations, homoclinic gluing, and Andronov–Hopf instabilities. Another example of alternating patterns appears in vertically vibrated fluids [13], where the profile of the fluid surface exhibits an hexagon-stripe-hexagon temporal sequence. Vibrated fluids are an example of parametrically driven systems, where the forcing mechanism oscillates in time.

Let us consider the particular case of driven magnetic systems. At nano-scales, magnetic devices can be kept out of the thermodynamic equilibrium by means of spin-transfer torques [15,16]. The spin-transfer torque effect is based on the interaction between the spins of the magnetic medium and the spins of the electric current. The dynamical responses of nanomagnets to spin-transfer torques include limit-cycles [17–19], magnetic reversals [19], chaos [20], patterns [21–23], vortex lattices [24,25], solitons [14,26], among others. This versatility of the spin-transfer torque renders it the ideal effect to manipulate magnetization, read and record information, and generate micro-frequency spin-waves [27]. Recently, a relationship between parametrically driven systems and nanomagnets forced with direct electric current has been established [14]. Moreover, both systems can be described by the same normal form equations and they show similar states such as solitons and patterns, even if the electric current is constant in time for the forced magnet. Therefore, driven nanomagnets can exhibit alternating patterns which are found in vibrated fluids.

The aim of this article is to study alternating superlattice textures in nanomagnets driven by spin-transfer torques. In particular, we focus on two states, superhexagons and square-like patterns. Using an appropriate modal decomposition of the magnetization equations, we show that the alternating superhexagons emerge through a homoclinic bifurcation. In the case of square-like patterns, the origin of the oscillations is a supercritical Andronov–Hopf instability. The article is organized as follows: in the next section we describe the physical system and the spatial instability responsible for pattern formation. In Section 3 we describe alternating superhexagons by means of direct numerical simulations and a modal decomposition. The last approach permits us to explain the emergence of dynamical patterns in terms of low-dimensional bifurcations. In Section 4 we study an oscillatory square-like state that emerges through an Andronov–Hopf instability. Finally, the conclusions are presented in Section 5.

2. Driven nanomagnets and magnetic textures formation

Let us consider a *spin-valve* device, which is metallic structure composed by two ferromagnets and one spacer between them. A schematic setup is shown in Fig. 1. Spin-valves usually have lateral dimensions of $L \sim 100$ nm. One ferromagnet is thicker than the other and it has a *fixed* magnetization that filters or polarizes the spins of the current towards the fixed magnetization direction **p**. The other ferrromagnet is a thin film known as *free* layer, and it interacts with the current and external fields. The rest of the structure is composed by conducting materials. We are interested in the dynamics of the free layer, which is described by its magnetization field vector $\mathbf{M} = \mathbf{M}(T, \mathbf{R})$. We consider two forcing mechanisms, namely an

external magnetic field $\mathbf{h_0} = h_0\mathbf{e}_x$ and a spin-transfer torque generated by an electric current g that flows perpendicular to the planes of the layers. The magnetization dynamics are described by the dimensionless *Landau–Lifshitz–Gilbert–Slonczewski equation* [15,28–30]

$$\frac{\partial\mathbf{m}}{\partial t} = -\mathbf{m}\times\left[(h_0+\beta_x m_x)\mathbf{e}_x - \beta_z m_z\mathbf{e}_z + \nabla^2\mathbf{m}\right] + g\mathbf{m}\times(\mathbf{m}\times\mathbf{e}_x) + \alpha\mathbf{m}\times\frac{\partial\mathbf{m}}{\partial t}, \tag{1}$$

where $\mathbf{m} = \mathbf{M}/M_s$ such that M_s is the saturation magnetization. The variables $t = T/(\gamma M_s)$ and $\mathbf{r} = \mathbf{R}/l_{ex} = x\mathbf{e}_x + y\mathbf{e}_y$ stand for the dimensionless time and space coordinates over the layer, respectively. Here the characteristic temporal γM_s and spatial l_{ex} scales are material properties. For example, for a cobalt layer of $3nm$ of thickness, $M_s \simeq 1.4\ 10^6$A/m, and the characteristic scales are $(\gamma M_s)^{-1} \simeq 3.2$ps, and $l_{ex} \simeq 3.4$ nm [28]. The gradient operator is defined as $\nabla \equiv \mathbf{e}_x\partial_x + \mathbf{e}_y\partial_y$. The unitary vectors $\{\mathbf{e}_x, \mathbf{e}_y, \mathbf{e}_z\}$ are oriented along the corresponding Cartesian axis (see Fig. 1).

In addition, the coefficients of anisotropy β_x and β_z stand for the preferred directions of the magnetization, and they are combinations of the magnetocrystalline and demagnetizing effects, moreover β_x (β_z) favors (disfavors) configurations along the x-axis (z-axis). The coefficient β_z is small for devices where the perpendicular magnetocristalyne anisotropy partially cancels the demagnetization effect (see [44] and references therein). The laplacian term accounts for the ferromagnetic exchange and it smoothes nonuniformities. The spin-polarized electric current is modeled by the term proportional to g, while α is a phenomenological dissipation coefficient. The sample borders are taken into account using Neumann boundary conditions for the magnetization. Both the external field $\mathbf{h_0}$ and the polarization of the current $\mathbf{p}$ are to point along the x-axis direction, which permits one to switch the magnetization between equilibria $\mathbf{m} = \mathbf{e}_x$ and $\mathbf{m} = -\mathbf{e}_x$. We focus here on the regime in which the electric current stabilizes the state $\mathbf{m} = \mathbf{e}_x$, and the external field disfavors it; this competition of forces induces rich spatiotemporal dynamics. Let us remark that, here we only consider the dominant order physical effects, however additional terms can be included into Eq. (1), such as the full non-local demagnetizing field [41], and variable spin-transfer torque amplitude $g = g(\mathbf{m})$ [29].

Eq. (1) has been extensively studied to explain and predict the emergence of limit-cycles [17–19], patterns [21–25], solitons [14,26], among other states. Notice that the magnetization norm is a conserved quantity, $\partial_t|\mathbf{m}|^2 = \partial_t\mathbf{m}\cdot\mathbf{m} = 0$, and therefore the magnetization can be written in different representations such as spherical [23,28], canonical [28] and stereographic [28,31]. In the last case, the spherical surface is mapped to the equatorial plane $m_x = 0$ through the relation $A = (m_y + im_z)/(1 + m_x)$. In this representation, A is a complex amplitude that accounts for the deviations from the $\mathbf{m} = \mathbf{e}_x$ solution. After straightforward calculation one obtains the following generalized *Complex Ginzburg–Landau* equation

$$(i+\alpha)\frac{\partial A}{\partial t} = (ig - h_a)A - \frac{\beta_z}{2}\left(A - \overline{A}\right)\frac{1+A^2}{1+|A|^2} - \beta_x A\frac{1-|A|^2}{1+|A|^2} + \nabla^2 A - 2\frac{\overline{A}}{1+|A|^2}(\nabla A)^2, \tag{2}$$

where $\bar{A}$ means the complex conjugate of A. The above model has been used to describe the dynamics of dissipative waves in several contexts [1,2]. An interesting limit of Eq. (2) is obtained for the scaling $\alpha \ll |A|^2 \sim \partial_t \sim \partial_{xx} \sim \beta_z \sim |g| \sim |v| \ll 1$ and $|h_a| \sim \beta_x \sim 1$, where $-v = h_0 + \beta_x + \beta_z/2$; in this case, the generalized Complex Ginzburg–Landau equation takes the form of the well-known *parametrically driven, damped nonlinear Schrödinger* equation,

$$\frac{\partial\bar{\psi}}{\partial t} = -iv\psi - i|\psi|^2\psi - i\nabla^2\psi - \mu\psi + \gamma\bar{\psi}, \tag{3}$$

where $\psi = \sqrt{2\beta_x}e^{i\pi/4}A$, $\mu = -g - \alpha v$, $\gamma = \beta_z/2$. The aforementioned equation has been used to describe several systems in presence of temporally-modulated forcings, known as parametrically driven systems. Furthermore, both driven nanomagnets and parametrically driven systems exhibit states such as localized states [32–41] and patterns [41–43]. This equivalence [14] between driven nanomagnets and parametrically forced systems suggests that the alternating textures found in vertically vibrated fluids [13] should also emerge in spin-transfer torque driven magnets.

Stationary patterns appear in spin-valves through a supercritical spatial instability of the uniform state $\psi = 0$ (see Refs. [14,23]). In this bifurcation, small perturbations with wavenumber $q^2 = v = -(h_0 + \beta_x + \beta_z/2)$ are amplified in time when $g \geq -\beta_z/2$. The existence of a real wavenumber $q^2 \geq 0$ is fulfilled when the external field is negative $h_0 \leq -(\beta_x + \beta_z/2) < 0$, that is, when the vector $\mathbf{h_0}$ points against the equilibrium $\mathbf{m} = \mathbf{e}_x$. Hence, patterns are the result of the competition between the spin-polarized current that stabilizes the $\psi = 0$ state and the external field that disfavors it ($h_0 < 0$). Using a normal form approach, it was obtained a general set of equations describing the temporal evolution of the critical modes [23]. This analysis revealed that for applied fields above a critical value, that is $h_0 > h_0^c \equiv -4(\beta_x + \beta_z/2)$, stripes are the only stable pattern. On the other hand, when the field is below the critical value $h_0 < h_0^c$, stationary superlattices emerge.

For negative external fields $h_0 < 0$, the electric current can switch the magnetization from $\mathbf{m} = +\mathbf{e}_x$ to $\mathbf{m} = -\mathbf{e}_x$ when g varies from negative to positive values. Hence, all the dissipative structures close to the equilibrium $\mathbf{m} = +\mathbf{e}_x$ in the phase space must become unstable when the current is increased. Indeed, increasing the control parameter g, which is equivalent to diminish dissipation [14] or increase injection, the system self-organizes into alternating superlattices (see Fig 2). The particular attractor usually depends on the external field h_0, the current g, the lateral dimension L and the initial condition. However, among the plethora of alternating textures that emerge in this system, two of them deserve special attention due to their regularity in Fourier space. The first one is the alternating superhexagon shown in Fig. 2, which is composed by six Fourier modes. We observe this texture for small applied fields close to $h_0 = -2.5$. The second alternating texture is a
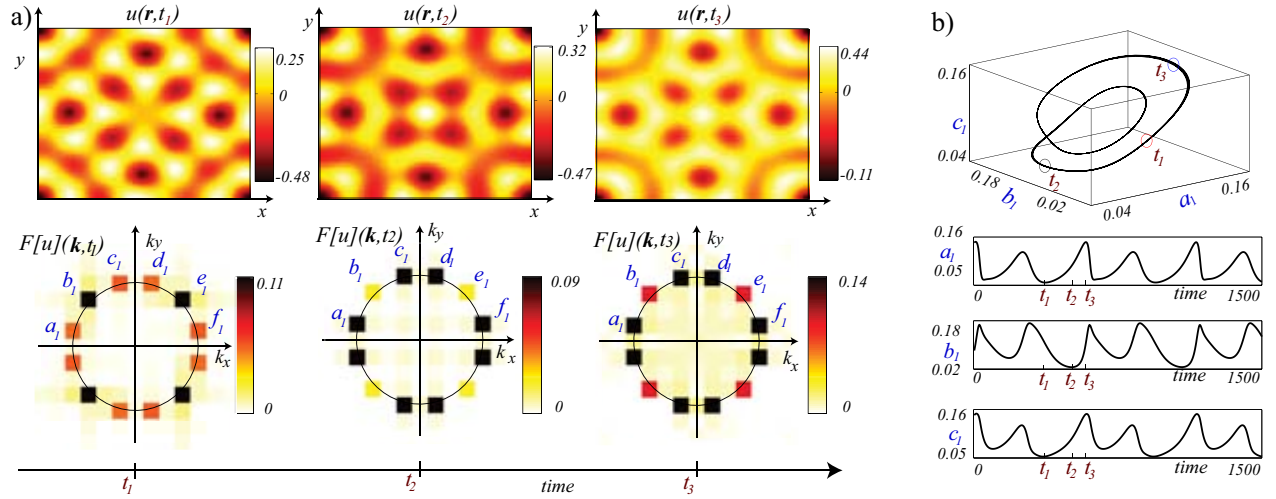
Fig. 2. Alternating superlattice state with six dominant Fourier modes (with their respective complex conjugate). (a) Three figures of a normalized magnetization component $u = m_y/(1 + m_x)$ are shown in the upper panel, while the lower panel illustrates the respective spatial Fourier spectra $F[u]$. The amplitude of the Fourier modes of u are $\{a_1, b_1, c_1, d_1, e_1, f_1\}$, we can define in a similar manner another reduced magnetization component, $v = m_z/(1 + m_x)$, and its respective Fourier amplitudes $\{a_2, b_2, c_2, d_2, e_2, f_2\}$. The modes oscillate between large and small values, moreover for the time t_2 the amplitude b_1 of the Fourier peak located on the diagonal almost disappears. (b) Trajectories $a_1(t)$, $b_1(t)$ and $c_1(t)$ are the envelopes of the modes shown in (a).
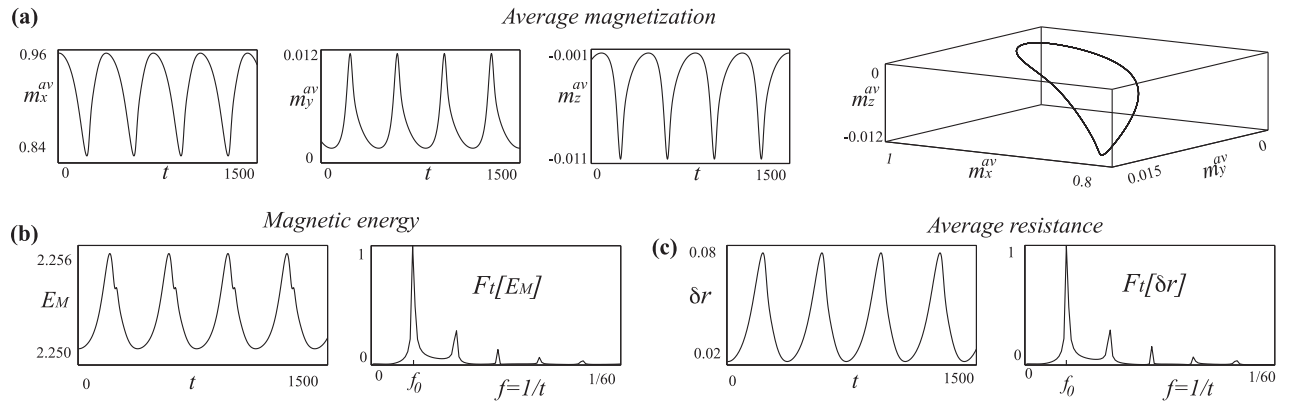

Fig. 3. Temporal evolution of the average magnetization, magnetic energy, and average resistance for $g = -0.4945$. (a) Components of the average magnetization vector $\mathbf{m}^{av}$. (b) Magnetic energy. The time series $E_M(t)$ is shown on the left, while the normalized temporal Fourier transform $F_t = F[E_M - < E_M >](f)$ is shown on the right panel, where $f = 1/t$ is the frequency. (c) Average resistance profile $\delta r(t)$ (left) and its normalized temporal Fourier transform $F_t[\delta r](f)$ (right).

square-like pattern state. Square-like states exhibit a spectrum with two large peaks and several smaller peaks (cf. Fig. 7). They appear for large applied fields close to $h_0 = -6$. These states emerges through an Andronov–Hopf bifurcation of the stationary square-like texture. The next two sections are devoted to the description of such states.

3. Alternating superhexagons

Let us consider applied fields close to $h_0 = -2.5$. In this case, the typical oscillatory state is composed by six interacting modes, which gives the appearance of a temporal alternation between patterns of different shapes, namely a square, a supersquare and a superhexagon. Fig. 2 illustrates this dissipative structure, which was obtained for the parameter values $g = -0.4911$, $\beta_x = 1/2$, $\beta_z = 1$, and $\alpha = 0.05$. The numerical simulation was conducted by dividing the sample into a grid of 90×90 squares of side length $dx = 0.230571$ (approximately 0.8 nm for cobalt). The spatial differential operators are approximated with centered schemes of order-6, while the time integration is performed using a fourth order Runge-Kutta algorithm with constant step-size $\Delta t = 0.01$ (approximately 0.03 ps for cobalt).

A simple physical quantity that characterizes the dynamics in time is spatial average of the magnetization, given by

$$\mathbf{m}^{av}(t) \equiv \frac{1}{L^2} \iint \mathbf{m}(t, \mathbf{r}) dx dy. \tag{4}$$

Fig. 3(a) shows the temporal evolution of this average. The oscillation period is around $\Delta t \sim 350$, which is about 1 ns for common devices. The trajectories are characterized by sharp peaks, moreover, they are far from the shape of sinusoidal
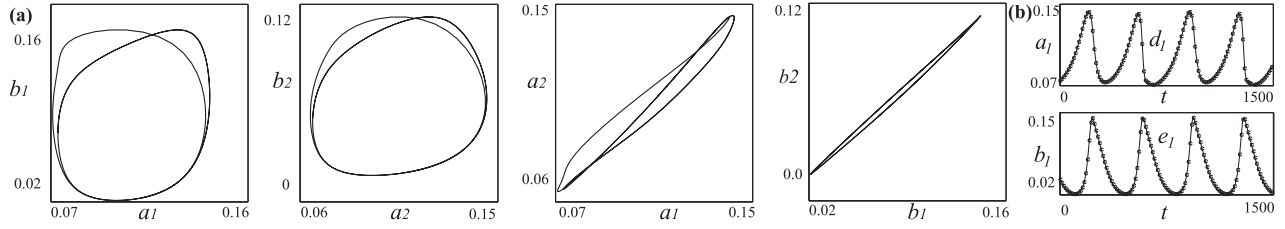
Fig. 4. Temporal evolution of the Fourier modes of an alternating superhexagon. (a) The magnetization is projected into the three Fourier modes a, b and c (cf.2). The graph of the left panel illustrates the general form of the phase space of alternating superhexagons. (b) Temporal series of the modes envelopes. The solid lines show a_1 (up) and b_1 (down), while the points stand for d_1 (up) and f_1 (down). Thus, the amplitudes of such modes are the same.

functions. This type of dynamical behavior suggests a homoclinic bifurcation as the creation mechanism of alternating super-hexagons [45]. In systems with a homoclinic bifurcation, a limit-cycle approaches a saddle-point when a control parameter is varied, the limit-cycle eventually collides with the hyperbolic fixed point and it disappears. The signature of this bifurcation is that the oscillations evolves slowly in the vicinity of the saddle-point or stagnation point [45].

A relevant quantity of ferromagnetic materials is the magnetic energy [28],

$$E_M = \frac{1}{L^2} \iint \left[-m_x h_0 - \frac{1}{2}\beta_x m_x^2 + \frac{1}{2}\beta_z m_z^2 + \frac{1}{2}\left(|\nabla m_x|^2 + |\nabla m_y|^2 + |\nabla m_z|^2\right) \right] dxdy. \tag{5}$$

The magnetic energy $E_M(t)$ is a global indicator that only depends in time, and then it provides information regarding the dynamics of the whole device. Fig. 3(b) shows the temporal evolution of the energy. The energy remains close to the energy of films uniformly magnetized along $\mathbf{m} = +\mathbf{e}_x$, that is $E_M^{+1} = -h_0 - \beta_x/2$. Let us define the normalized Fourier spectrum of the magnetic energy as

$$F_t \equiv F_t[E_M - < E_M >](f), \tag{6}$$

where F_t is the normalized Fourier transform (that is, its maximum value is 1), and $< E_M >$ is the energy mean value. The spectra are characterized by one dominant peak at a frequency of $f_0 = 2.77 \times 10^{-3}$ (which is in the Gigahertz domain for typical devices), and several harmonic peaks at frequencies nf_0, where $n = 2, 3, ...$

Another relevant dynamical indicator is the reduced magnetoresistance of the device,

$$\delta r \equiv \frac{R[m_x] - R[1]}{R[-1] - R[1]} = \frac{1}{L^2} \iint \frac{1 - m_x}{2} dxdy, \tag{7}$$

where R is the electrical resistance of the spin-valve, which can be measured experimentally. The spatial average used in formula (7) is the generalization of the magnetoresistance calculated for uniformly magnetized free layers. Fig. 3(c) illustrates the behavior of the reduced resistance and its normalized Fourier spectrum (obtained with an expression similar to formula (6)). Hence, the signature of alternating super-hexagons is a dominant frequency close to f_0 in the magnetoresistance.

Let us focus on the modal decomposition of Fig. 2. In the context of nanomagnetism the device lateral dimensions are small, that is $L \sim 50 - 100nm$, and then a few wavenumbers are admitted inside the ferromagnetic layer; this favors a defect-free texture. Moreover, as the lower panel of Fig. 2 shows, the dominant Fourier peaks are close to the critical wavenumber of the spatial instability $|\mathbf{k}| \approx q$, while the amplitude of the other modes are negligible. This is because the primary and the secondary bifurcations, responsible of the emergence of stationary and oscillatory patterns respectively, occur for close values of the electric current. The Fourier spectrum is characterized by large peaks at the following wavevectors $\mathbf{q_1} = \Delta k(-4, 1)$, $\mathbf{q_2} = \Delta k(-1, 4)$, $\mathbf{q_3} = \Delta k(1, 4)$, $\mathbf{q_4} = \Delta k(4, 1)$, $\mathbf{Q_1} = \Delta k(-3, 3)$, and $\mathbf{Q_2} = \Delta k(3, 3)$, and their negative counterparts. The geometrical factor $\Delta k = 2\pi/L$ accounts for the minimal wavenumber that is admitted by the boundary conditions.

We observe that the envelopes of the pattern evolve in twin pairs, that is, $a_1 = d_1$, $b_1 = e_1$, and $c_1 = f_1$. Fig. 4(b) illustrates the typical correlated trajectories. The same holds for the spectrum of the imaginary part of A, that is, $a_2 = d_2$, $b_2 = e_2$, and $c_2 = f_2$. Therefore, the effective degrees of freedom of this system are the amplitudes of three interacting square lattices. Fig. 2(b) shows the temporal evolution of the envelopes of each square.

The texture oscillations become slower and more regular when the electric current approaches the value $g_c = -0.4953$. Moreover, for electric currents below the critical value g_c, the limit-cycle is not observed and the magnetization self-organizes into a stationary pattern. In this region, the numerical integration of the system is time-consuming, which makes difficult to elucidate the formation mechanism of the alternating structures. In the next subsection we obtain a reduced representation of the superhexagon by means of a Galerkin expansion.

3.1. Four-modes Galerkin expansion

The normal form approach allows one to obtain a set of amplitude equations $dA_j/dt = -\delta H/\delta \bar{A}_j$ for different types of patterns [23], where the Lyapunov function H is minimized along the evolution of the system. This method permits one to
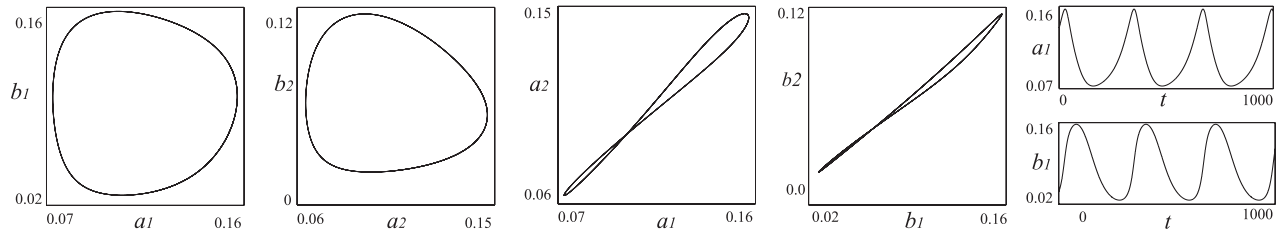
Fig. 5. Phase portrait of Galerkin modes. (a) limit-cycle in the modes representation. (b) Trajectories of the Galerkin modes.
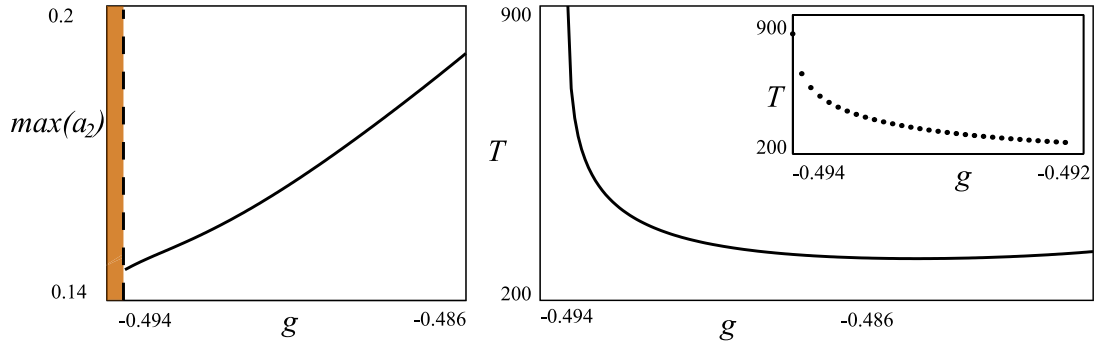

Fig. 6. Characteristic limit-cycle amplitude (left) and period (right). There is no limit-cycle for electric currents below a threshold (darker zone in the amplitude plot), the oscillations emerge abruptly for $g = -0.494$. At the onset of the emergence of the oscillations, the amplitude is finite and the period T has a logarithmic divergence. The inset shows a comparison between the data of the numerical integration (dots) and fitting curve $T \simeq 113.21 \log[1/(g + 0.49361)] - 398.54$.

characterize stationary structures at the onset of the bifurcation, however, permanent behaviors, such as chaos and oscillations, are forbidden. Another strategy to simplify the dynamics is to project the equations into a few relevant modes, a Galerkin expansion. This type of modal decomposition allows the study permanent dynamics, because they are not subjected to the minimization of a Lyapunov function [5].

Following the Galerkin approach of Ref. [5], we decompose the spatiotemporal magnetization dynamics into a few trajectories for the relevant observed modes, using the following ansatz for the stereographic projection $A(t, \mathbf{r}) = A_r + iA_i$

$$\begin{pmatrix} A_r \\ A_i \end{pmatrix} = \begin{pmatrix} -a_1 \\ a_2 \end{pmatrix} [\cos(\mathbf{q_1} \cdot \mathbf{r}) + \cos(\mathbf{q_2} \cdot \mathbf{r}) + \cos(\mathbf{q_3} \cdot \mathbf{r}) + \cos(\mathbf{q_4} \cdot \mathbf{r})] + \begin{pmatrix} -b_1 \\ b_2 \end{pmatrix} [\cos(\mathbf{Q_1} \cdot \mathbf{r}) + \cos(\mathbf{Q_2} \cdot \mathbf{r})],$$

(8)

where the real-valued functions $a_1(t)$ and $a_2(t)$ are the envelopes of the supersquare pattern given by the wavevectors $\{\mathbf{q_1}, \mathbf{q_2}, \mathbf{q_3}, \mathbf{q_4}\}$. For the sake of simplicity, we use the same amplitude for the square sub-lattices given by $\{\mathbf{q_1}, \mathbf{q_3}\}$ and $\{\mathbf{q_2}, \mathbf{q_4}\}$. The variables $b_1(t)$ and $b_2(t)$ are the real-valued amplitudes of the square pattern defined by the wavevectors $\{\mathbf{Q_1}, \mathbf{Q_2}\}$. Writing Eq. (2) into its real and imaginary parts, using expression (8), and projecting over the spatial modes (using the inner product for Fourier spaces), we obtain a simple dynamical system of the form

$$\frac{d\mathbf{X}}{dt} = \mathbf{F}(\mathbf{X}),$$

(9)

where $\mathbf{X} = (a_1, a_2, b_1, b_2)^T$. Due to the long expression of $\mathbf{F}$, its explicit form and the details of the projection method are given in Appendix A. In order to understand and characterize the origin mechanism of the alternating superlattice states described in Section 3, we integrate the set of Eqs. (9) using a fifth-order Runga–Kutta routine with variable step size and the same parameter values as in Section 3. Fig. 5 shows the typical limit-cycle solution obtained for $g = -0.4911$. The trajectories are characterized by a slow motion in a determined region of the phase space (stagnation point, close to $a_1 = a_2 = 0$), moreover, when the current is decreased, the time that the trajectories spend in this region is increased.

Notice that we use an ansatz with only four amplitudes, which is the minimal modal decomposition that permits obtaining qualitative agreement with the magnetic equations and, at the same time, provides the possibility to identify the formation mechanism of superhexagons. A more general decomposition with more modes is required to obtain a better quantitative agreement with the magnetic equations. However, this four-modes expansion is complete enough to obtain information of the alternating superhexagons.

The characteristic limit-cycle amplitude and period are shown in Fig. 6. As it can be seen, the amplitude appears abruptly, which agrees with the direct numerical simulations of the magnetic equations. Moreover, decreasing the control parameter g, the oscillation period diverges with a logarithmic law $T \simeq 113.21 \log[1/(g - g_c)] - 398.54$, where $g_c = -0.49361$. This particular divergence law permits us to conclude that the mechanism is a homoclinic bifurcation.
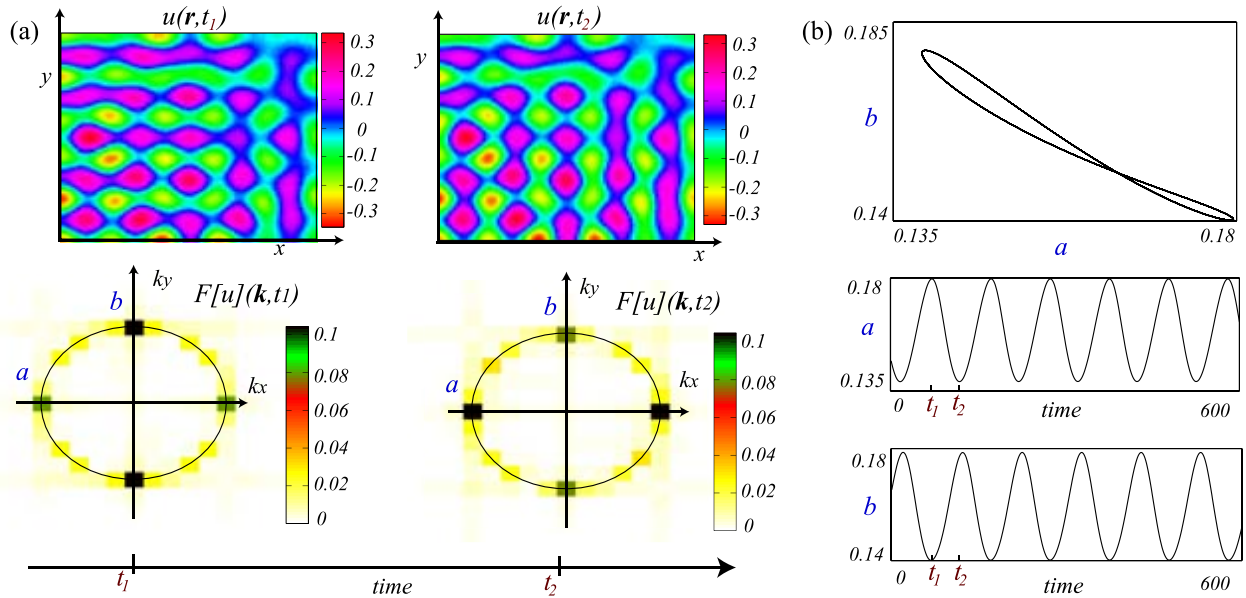
Fig. 7. Oscillatory square-like state obtained for $h_0 = -6$ and $g = -0.41$. (a) Plots of u, the real part of A (upper panel) and its respectively spatial Fourier transform (bottom panel). (b) Projection of trajectory in envelopes space and temporal evolution of the dominant envelopes.
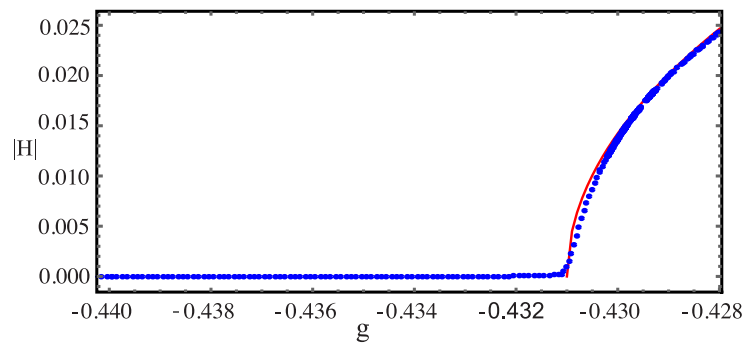

Fig. 8. Oscillation amplitude for square-like alternating texture. The oscillation envelope obeys a law $|H| = (g - g'_c)^{1/2}$, this curve is plotted in solid line. Points account for the data of the direct numerical simulation.

The Galerkin expansion **f** will have only odd nonlinearities because model (2) is invariant under inversions of the order parameter ($A \rightarrow -A$). According to our simulations, the quintic term is necessary to observe limit-cycles. Therefore, the relevant nonvariational interaction between modes occurs through a coupling of fifth order.

In the previously studied spin-transfer torque induced limit-cycles [17–19], the dissipation α plays an important role. Indeed, limit-cycles are the result of the balance between the dissipation α and the injection $g > 0$. However, in the case of alternating superlattices, we observe that the dissipation coefficient α does not produce relevant changes in the dynamics. Furthermore, in the limit $\alpha = 0$ the oscillatory states do not change appreciably. Hence, we conclude that the spin-transfer torque is the dominant dissipation mechanism of alternating superlattices.

4. Oscillatory square-like texture

A different scenario occurs for large applied external fields, where the alternating patterns are composed by a few dominant modes. For external fields around $h_0 = -6$, the typical oscillatory structure is a square-like pattern. Fig. 7 illustrates this texture which was obtained for $g = -0.41$, and spatial and temporal step-sizes are $dx = 0.157861$ (approximately 0.51 nm) and $\Delta t = 0.004$ (approximately 0.013 ps), respectively. As it can be seen from this figure, the envelopes of the horizontal and the vertical rolls oscillate in time. The two rolls have orthogonal wavevectors $\mathbf{q_1} = q(1,0)$, $\mathbf{q_2} = q(0,1)$, where q is the critical wavenumber of the spatial instability found in Ref. [23]. This oscillatory state is similar to the one observed in fluids heated from bellow [3,4], where the two-mode texture oscillates in time.

The temporal evolution of the two dominant modes is approximately sinusoidal [see Fig. 7(b)], with period around $\Delta t = 100$, which is about 0.32 ns for cobalt. In addition, the amplitude of the temporal oscillation of each mode decreases monotonically when g is decreased, until the oscillations disappear at $g'_c \approx -0.43$, see Fig. 8. These two features are the sig-
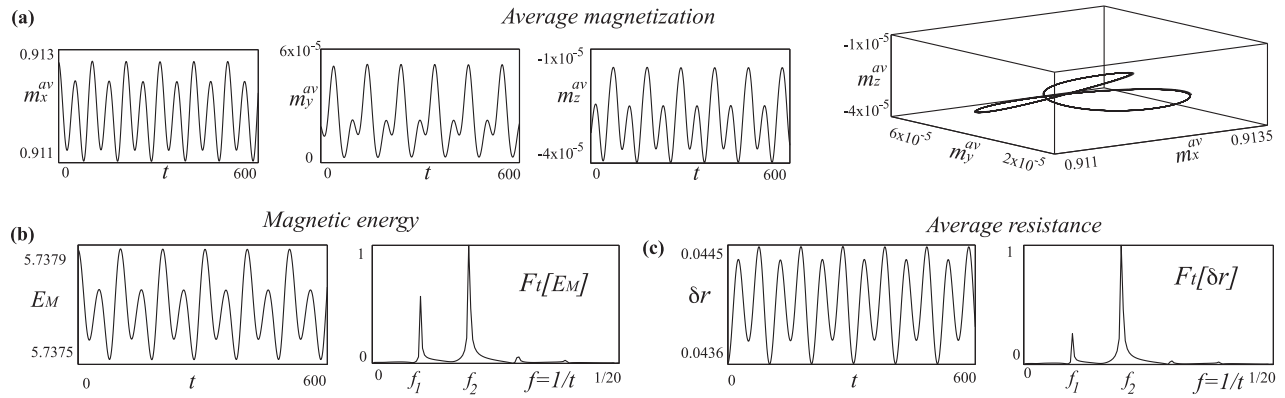
Fig. 9. Temporal evolution of the average magnetization, magnetic energy, and average resistance for $g = -0.41$. (a) Components of the average magnetization vector. (b) Magnetic energy. The time series $E_M(t)$ is shown on the left, while the temporal Fourier transform $F_t = F[E_M - <E_M>](f)$ is shown on the right panel. (c) Average resistance profile $\delta r(t)$ (left) and its temporal Fourier transform $F_t[\delta r - <\delta r>](f)$ (right).

nature of a supercritical Andronov–Hopf bifurcation [45]. This instability is usually characterized by the complex Ginzburg–Landau equation, which contains the dominant order terms compatible with the symmetries of the physical system and the instability [1]

$$\frac{dH}{dt} = (g - g_c')H - (\Gamma_0 + ic)H|H|^2, \tag{10}$$

where the order parameter $H(t)$ stands for the oscillation envelope, Γ_0 is the nonlinear coefficient, which is positive. The parameter c accounts for the coupling between the oscillation frequency and amplitude. The stationary solutions of the above model have modulus $|H| = [(g - g_c')/\Gamma_0]^{1/2}$. Fig. 8 shows the solution of the Ginzburg–Landau model using $\Gamma_0 = 4.9383$ (solid line) and the oscillation envelope obtained from direct numerical simulations of the magnetic equations (points). The agreement is fairly good.

The oscillations of the magnetization spatial average $\mathbf{m}^{av}(t)$ are shown in Fig. 9(a) and they are very close to the steady state $\mathbf{m} = +\mathbf{e}_x$. Notice that the nonlinear transformation between the dynamical variables (stereographic representation) and the Cartesian components

$$(m_x, m_y, m_z) = \frac{1}{1 + |A|^2}\left(1 - |A|^2, A + \bar{A}, i[\bar{A} - A]\right), \tag{11}$$

generates additional frequencies (harmonics) in the temporal Fourier spectrum. Hence, both the magnetic energy and the average resistance will have extra frequencies. Fig. 9(b) shows the temporal evolution of the energy, which again is close to the value $E_M^{+1} = -h_0 - \beta_x/2$. The energy spectrum is characterized by two dominant peaks at a frequency of $f_1 = 0.01$ and $f_2 = 2f_1$ (which is in the gigahertz domain for typical devices), and several other peaks at frequencies nf_1, where $n = 2, 3, ..$; Fig. 9(c) illustrates the behavior of the average resistance and its normalized Fourier spectrum.

5. Conclusions and remarks

In recent decades, most scientific efforts have concentrated on understanding primary spatial instabilities. However, due to the complex spatiotemporal behavior exhibited by secondary instabilities, several questions still remain unanswered. Here, we have investigated alternating superlattices—oscillatory patterns with several Fourier modes—induced by spin-transfer torques. The envelopes of the modes alternate between small and large values, which produces textures of different shapes. We focused mainly on alternating superhexagons and square-like patterns, which are oscillatory states composed by six and two dominant spatial modes, respectively. Using a simple modal decomposition, we showed that superhexagons emerge through a homoclinic bifurcation. We have considered only four modes and it provides a qualitative understanding of the dynamics. Notice that in the present case, it is necessary to use several modes to get a better quantitative agreement. Moreover, the lack of control expansion coefficient in the Galerkin method renders it a less precise strategy than amplitude equations. To have a deep unified understanding of the dynamic behavior of secondary bifurcations, novel concepts and theoretical tools are required, which represents a challenge to nonlinear science.

For large applied fields, square-like states emerge. They have two dominant Fourier modes that oscillate harmonically. The mechanism that originates the square-like patterns is a supercritical Andronov–Hopf instability. This texture is similar to the ones reported previously for the Rayleigh–Bénard experiments [3,4]. We expect that increasing the electric current will induce complex dynamical behaviors, such as chaos and spatiotemporal chaos, in the textures. Work in this direction is in progress.

The observation of alternating patterns in nanomagnetism enforces the hypothesis regarding the equivalence between driven nanomagnets and systems with time-dependent forcing, namely parametrically driven systems. Moreover, alternating

patterns offers the opportunity to generate and eventually manipulate a wide variety of spin-waves in the gigahertz domain. On the one hand, this promises to increase the technological applications of spin-valve devices, on the other hand, it becomes necessary to study alternating patterns using more general and more realistic approaches. Some generalizations include the use of circular or elliptical devices, a complete treatment of the non-local demagnetizing fields, the use of thermal torques, among others; work in this direction is left as an open problem.

Acknowledgment

Appendix A. Galerkin expansion of the magnetization equations

Due to the spatial regularity of the alternating superhexagons, we introduce the following ansatz

$$
\begin{aligned}
A_r ={}& a_1[\cos(\mathbf{q_1}\cdot\mathbf{r}+\gamma_{r1})+\cos(\mathbf{q_2}\cdot\mathbf{r}+\gamma_{r2})+\cos(\mathbf{q_3}\cdot\mathbf{r}+\gamma_{r3})+\cos(\mathbf{q_4}\cdot\mathbf{r}+\gamma_{r4})]\\
&+ b_1[\cos(\mathbf{Q_1}\cdot\mathbf{r}+\Gamma_{r1})+\cos(\mathbf{Q_2}\cdot\mathbf{r}+\Gamma_{r2})],\\
A_i ={}& a_2[\cos(\mathbf{q_1}\cdot\mathbf{r}+\gamma_{i1})+\cos(\mathbf{q_2}\cdot\mathbf{r}+\gamma_{i2})+\cos(\mathbf{q_3}\cdot\mathbf{r}+\gamma_{i3})+\cos(\mathbf{q_4}\cdot\mathbf{r}+\gamma_{i4})]\\
&+ b_2[\cos(\mathbf{Q_1}\cdot\mathbf{r}+\Gamma_{i1})+\cos(\mathbf{Q_2}\cdot\mathbf{r}+\Gamma_{i2})],
\end{aligned}\tag{A.1}
$$

where the functions $\{a_1(t),\,a_2(t),\,b_1(t),\,b_2(t)\}$ are the magnitude of the amplitude of the respective mode, and $\{\gamma_{rj}(t),\,\gamma_{ij}(t),\,\Gamma_{ik}(t),\,\gamma_{ik}(t)\}$ for $j=1,2,3,4$ and $k=1,2$, are the phases of the modes. Since we consider Neumann boundary conditions, the admissible values for the phases are 0 and π. We use here the numerically observed values of the phases: $\gamma_{r1}(t)=\gamma_{r2}(t)=\gamma_{r3}(t)=\gamma_{r4}(t)=\Gamma_{r1}(t)=\Gamma_{r2}(t)=\pi$, and $\gamma_{i1}(t)=\gamma_{i2}(t)=\gamma_{i3}(t)=\gamma_{i4}(t)=\Gamma_{i1}(t)=\Gamma_{i2}(t)=0$. In this case, the ansatz (A.1) reduces to formula (8). Writing Eq. (2) into its real and imaginary parts, $\partial_t A = G_r + iG_i$, using ansatz (A.1) or equivalently (8), and considering the inner product for Fourier spaces, we obtain after straightforward calculations the following set of Eqs.,

$$
\begin{aligned}
8\dot a_1 \equiv{}& \frac{8}{L^2}\int\int\cos(\mathbf{q_1}\cdot\mathbf{r})G_r(\mathbf{r},a_1,a_2,b_1,b_2)dxdy\\
={}& -\Delta k^2[2176b_1^5+6690a_1a_2b_1^2b_2+b_1^3(-476+4352a_1^2-649a_2^2+3885b_2^2)\\
&+2a_1a_2b_2(1189a_1^2+144(-2+3a_2^2+3b_2^2))]\\
&-\Delta k^2[b_1(2176a_1^4+a_1^2(-476+1507a_2^2+1729b_2^2)-8(17+27a_2^4+36b_2^2-81b_2^4-18a_2^2(2+3b_2^2)))]+8b_1\beta_x\\
&-84a_1^2b_1\beta_x+640a_1^4b_1\beta_x-16a_2^2b_1\beta_x+666a_1^2a_2^2b_1\beta_x+36a_2^4b_1\beta_x-84b_1^3\beta_x+1280a_1^2b_1^3\beta_x+222a_2^2b_1^3\beta_x\\
&+640b_1^5\beta_x-32a_1a_2b_2\beta_x+444a_1^3a_2b_2\beta_x+144a_1a_2^3b_2\beta_x+1332a_1a_2b_1^2b_2\beta_x-48b_1b_2^2\beta_x+666a_1^2b_1b_2^2\beta_x\\
&+216a_2^2b_1b_2^2\beta_x+1110b_1^3b_2^2\beta_x+144a_1a_2b_2^3\beta_x+180b_1b_2^4\beta_x+8b_1\beta_z-84b_1^3\beta_z+640a_1^2b_1^3\beta_z+111a_2^2b_1^3\beta_z\\
&+640b_1^5\beta_z+666a_1a_2b_1^2b_2\beta_z-48b_1b_2^2\beta_z+333a_1^2b_1b_2^2\beta_z+108a_2^2b_1b_2^2\beta_z+1110b_1^3b_2^2\beta_z+72a_1a_2b_2^3\beta_z\\
&+180b_1b_2^4\beta_z+8a_1\,g+8b_1h_0-\alpha\{128a_1^5(-17\Delta k^2+5\beta_x)+6a_1^2a_2b_1b_2(-1115\Delta k^2+111(2\beta_x+\beta_z))\\
&+a_1^3(\Delta k^2(476-3885a_2^2-4352b_1^2+649b_2^2)-84\beta_x+1110a_2^2\beta_x+(640b_1^2+111b_2^2)(2\beta_x+\beta_z))+8a_1(\beta_x+h_0)\\
&+2b_1(36a_2^3b_2(-12\Delta k^2+2\beta_x+\beta_z)+a_2b_2(\Delta k^2(288-1189b_1^2-432b_2^2)+2(-8+111b_1^2+36b_2^2)(\beta_x+\beta_z))-4\,g)\\
&+a_1(-\Delta k^2(648a_2^4+68(-2-7b_1^2+32b_1^4)+(288+1507b_1^2)b_2^2-216b_2^4+a_2^2(-288+1729b_1^2+432b_2^2))+180a_2^4\beta_x\\
&+2(320b_1^4-8b_2^2+18b_2^4+b_1^2(-42+333b_2^2))(\beta_x+\beta_z)+3a_2^2(2(-8+111b_1^2+36b_2^2)\beta_x+3(37b_1^2+12b_2^2)\beta_z))\},
\end{aligned}\tag{A.2}
$$

where $\dot f = df/dt$. Other envelopes are calculated in a similar way

$$
4\dot a_2 \equiv \frac{4}{L^2}\int\int\cos(\mathbf{q_1}\cdot\mathbf{r})G_i(\mathbf{r},a_1,a_2,b_1,b_2)dxdy,\tag{A.3}
$$

$$
8\dot b_1 \equiv \frac{8}{L^2}\int\int\cos(\mathbf{Q_1}\cdot\mathbf{r})G_r(\mathbf{r},a_1,a_2,b_1,b_2)dxdy,\tag{A.4}
$$

$$
4\dot b_2 \equiv \frac{4}{L^2}\int\int\cos(\mathbf{Q_1}\cdot\mathbf{r})G_i(\mathbf{r},a_1,a_2,b_1,b_2)dxdy,\tag{A.5}
$$

and the resulting equations (not shown) have the same structure of Eq. (A.2). We remark that, the partial differential equation that describes magnetic media was reduced to a set of ordinary differential equations with four variables. This decomposition admits a geometrical description of the oscillations, and an efficient numerical characterization. A more general ansatz involving more modes might be used to obtain a better quantitative agreement with the magnetic equations. However, this four-modes expansion is complete enough to obtain a qualitative description of the alternating superhexagons.

References

[1] Cross MC, Hohenberg PC. Pattern formation outside of equilibrium. Rev Mod Phys 1993;65:851.
[2] Hoyle RB. Pattern formation:an introduction to methods. Cambridge University Press; 2006.
[3] Le Gal P, Pocheau A, Croquette V. Square versus roll pattern at convective threshold. Phys Rev Lett 1985;54:2501-2505.
[4] Moses E, Steinberg V. Competing patterns in a convective binary mixture. Phys Rev Lett 1986;57:2018-2021.
[5] Müller HW, Lücke M. Competition between roll and square convection patterns in binary mixtures. Phys Rev A 1988;38:2965-2974.
[6] Huke B, Lücke M. Roll, square, and cross-roll convection in ferrofluids. J Magn Mag Mater 2005;289:264-267.
[7] Weggler S, Huke B, Lücke M. Roll and square convection in binary liquids: A few-mode galerkin model. Phys Rev E 2010;81:016309.
[8] Pharasi HK, Kumar K. Oscillatory instability and fluid patterns in low-prandtl-number Rayleigh-beÈîÃünard convection with uniform rotation. Phys Fluids 2013;25:104105.
[9] Pal P, Kumar K, Maity P, Dana SK. Pattern dynamics near inverse homoclinic bifurcation in fluids. Phys Rev E 2013;87:023001.
[10] Maity P, Kumar K, Pal P. Homoclinic bifurcations in low-prandtl-number Rayleigh–Benard convection with uniform rotation. Eur Phys Lett 2013;103:64003.
[11] Maity P, Kumar K. Zero-prandtl-number convection with slow rotation. Phys Fluids 2014;26:104103.
[12] Dan S, Pal P, Kumar K. Low-prandtl-number Rayleigh–Benard convection with stress-free boundaries. Eur Phys J B 2014;87:278.
[13] Périnet N, Juric D, Tuckerman LS. Alternating hexagonal and striped patterns in faraday surface waves. Phys Rev Lett 2012;109:164501.
[14] Leon AO, Clerc MG. Spin-transfer-driven nano-oscillators are equivalent to parametric resonators. Phys Rev B 2015;91:01441.
[15] Slonczewski JC. Current-driven excitation of magnetic multilayers. J Magn Mag Mater 1996;159:L1.
[16] Berger L. Emission of spin waves by a magnetic multilayer traversed by a current. Phys Rev B 1996;54:9353.
[17] Kiselev SI, Sankey JC, Krivorotov IN, Emley NC, Schoelkopf RJ, Buhrman RA, et al. Microwave oscillations of a nanomagnet driven by a spin-polarized current. Nature 2003;425:380.
[18] Slavin A, Tiberkevich V. Nonlinear auto-oscillator theory of microwave generation by spin-polarized current. IEEE Trans Mag 2009;45:1875.
[19] Lee KJ, Deac A, Redon O, Nozieres JP, Dieny B. Excitations of incoherent spin-waves due to spin-transfer torque. Nat Mater 2004;3:877.
[20] Berkov D, Gorn N. Transition from the macrospin to chaotic behavior by a spin-torque driven magnetization precession of a square nanoelement. Phys Rev B 2005;71:052403.
[21] Volkov OM, Kravchuk VP, Sheka DD, Mertens FG, Gaididei Y. Periodic magnetic structures generated by spinpolarized currents in nanostripes. Appl Phys Lett 2013;103:222401.
[22] Kravchuk VP, Volkov OM, Sheka DD, Gaididei Y. Periodic magnetization structures generated by transverse spin current in magnetic nanowires. Phys Rev B 2013;87:224402.
[23] Leon AO, Clerc MG, Coulibaly S. Dissipative structures induced by spin-transfer torques in nanopillars. Phys Rev E 2014;89:022908.
[24] Volkov OM, Kravchuk VP, Sheka DD, Gaididei Y. Spin-transfer torque and current-induced vortex superlattices in nanomagnets. Phys Rev B 2011;84:052404.
[25] Gaididei Y, Volkov OM, Kravchuk VP, Sheka DD. Magnetic vortex-antivortex crystals generated by spin-polarized current. Phys Rev B 2012;86:144401.
[26] Li ZD, Li QY, Li L, Liu W. Soliton solution for the spin current in a ferromagnetic nanowire. Phys Rev E 2007;76:026605.
[27] Stiles MD, Miltat J. Spin dynamics in confined magnetic structures III. Springer; 2006.
[28] Mayergoyz ID, Bertotti G, Serpico C. Nonlinear magnetization dynamics in nanosystems. Elsevier; 2009.
[29] Xiao J, Zangwill A, Stiles M. Macrospin models of spin transfer dynamics. Phys Rev B 2005;72:014446.
[30] Ralph DC, Stiles MD. Spin transfer torques. J Magn Mag Mater 2008;320:1190.
[31] Lakshmanan M. The fascinating world of the Landau–Lifshitz–Gilbert equation: an overview. Philos Trans R Soc A 2011;369:1280.
[32] Barashenkov IV, Zemlyanaya EV. Stable complexes of parametrically driven, damped nonlinear Schrödinger solitons. Phys Rev Lett 1999;83:2568.
[33] Clerc MG, Coulibaly S, Laroze D. Nonvariational isingbloch transition in parametrically driven systems. Int J Bifur Chaos 2009;19:2717.
[34] Clerc MG, Coulibaly S, Laroze D. Parametrically driven instability in quasi-reversal systems. Int J Bifur Chaos 2009;19:3525.
[35] Clerc MG, Coulibaly S, Laroze D. Interaction law of 2d localized precession states. Eur Phys Lett 2010;90:38005.
[36] Clerc MG, Coulibaly S, Laroze D. Effective-parametric resonance in a non-oscillating system. Eur Phys Lett 2012;98:30006.
[37] Urzagasti D, Laroze D, Clerc MG, Coulibaly S, Pleiner H. Two-soliton precession state in a parametrically driven magnetic wire. J Appl Phys 2012;111:07D111.
[38] Urzagasti D, Laroze D, Clerc MG, Pleiner H. Breather soliton solutions in a parametrically driven magnetic wire. Eur Phys Lett 2013;104:40001.
[39] Urzagasti D, Aramayo A, Laroze D. Solitonantisoliton interaction in a parametrically driven easy-plane magnetic wire. Phys Lett A 2014;378:2614.
[40] Urzagasti D, Laroze D, Pleiner H. Localized chaotic patterns in weakly dissipative systems. Eur Phys J ST 2014;223:141.
[41] Clerc MG, Coulibaly S, Laroze D, Leon AO, Núñez AS. Alternating spin-polarized current induces parametric resonance in spin valves. Phys Rev B 2015;91:224426.
[42] Miles JW. Parametrically excited solitary waves. J Fluid Mech 1984;148. 451.T
[43] Kahouadji L, Périnet N, Tuckerman S, Shin S, Chergui J, Juric D. Numerical simulation of supersquare patterns in faraday waves. J Fluid Mech 2015;772:R2.
[44] Ralph DC, Cui YT, Liu LQ, Moriyama T, Wang C, Buhrman RA. Spin-transfer torque in nanoscale magnetic devices. Philos Trans R Soc A 2011;369:3617-3630.
[45] Strogatz SH. Nonlinear dynamics and chaos:with applications to physics, biology, chemistry, and engineering. Westview Press; 2001.